J. Fluid Mech. (2023), *vol*. 958, A22, doi:10.1017/jfm.2023.77

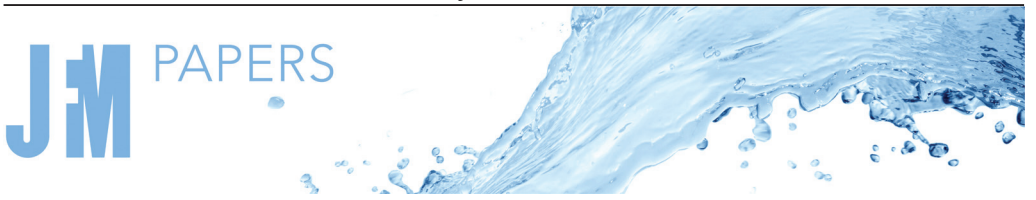

Surface wave instability in the thermocapillary migration of a flat droplet

Kai-Xin Hu[1],†, **Shao-Neng Zhang**[1] **and Qi-Sheng Chen**[2,3]

[1]Zhejiang Provincial Engineering Research Center for the Safety of Pressure Vessels and Pipelines, Faculty of Mechanical Engineering and Mechanics, Ningbo University, Ningbo, Zhejiang 315211, PR China

[2]School of Engineering Science, University of Chinese Academy of Sciences, Beijing 100190, PR China

[3]Key Laboratory of Microgravity, Institute of Mechanics, Chinese Academy of Sciences, Beijing 100190, PR China

(Received 3 May 2022; revised 12 September 2022; accepted 16 January 2023)

The surface wave instability (SWI) of thermocapillary migration is examined by linear stability analysis for a droplet on a unidirectional heated plane. Both a Newtonian fluid and an Oldroyd-B fluid are considered. The droplet, flattened by gravity, is susceptible to two kinds of instabilities: convective instability (CI), which is independent of surface deformation; and SWI, which occurs only when the Galileo number and the surface-tension number are not too large. The wavenumber of the latter is much smaller than that of the former, while the reverse is true for the wave speed. SWI is found at different Prandtl numbers (Pr), while its mode includes streamwise and oblique waves. Energy analysis suggests that the energy of the long-wave mode comes from the shear stress induced by the surface deformation, the energy source for the mode with finite wavelength is the work done by Marangoni forces, while the energy from the basic flow is only important in some cases at small Pr. For the Oldroyd-B fluid, a small elasticity slightly changes the critical Marangoni number of SWI, while larger elasticity changes the preferred mode from SWI to CI. The instability mechanism is discussed and comparisons are made with experimental results.

Key words: thermocapillarity, shear-flow instability, thin films

1. Introduction

The migration of a droplet placed on a non-uniformly heated solid surface can be driven by the temperature-induced surface tension gradient. This phenomenon is called thermocapillary migration, which appears in a variety of microfluidic applications

† Email address for correspondence: hukaixin@nbu.edu.cn

(Karbalaei, Kumar & Cho 2016). For example, thermocapillary migration has been used in a microfluidic device for droplet and liquid stream actuation on a chemically patterned substrate by Darhuber *et al.* (2003). They have also proposed a device for droplet production with controlled size (Darhuber, Valentino & Troian 2010). In addition, several thermocapillary-based microfluidic platforms have been proposed for droplet displacing, switching and trapping (Selva *et al.* 2010), sensing droplet position, size and composition (Chen *et al.* 2004), detection and analysis (Valentino, Troian & Wagner 2005), etc.

Thus, abundant works including theoretical, numerical and experimental studies (Shankar Subramanian & Balasubramaniam 2005; Pratap, Moumen & Subramanian 2008; Liu & Zhang 2015; Wu 2018) have been carried out on thermocapillary migration due to its practical importance. Dai *et al.* (2021) have reviewed recent advances in the fundamentals, evaluations and manipulation strategies in this field.

Several authors have presented theoretical models of thermocapillary migration. Brochard (1989) has investigated the motions of droplets on solid surfaces induced by chemical or thermal gradients, and obtained an analytical expression for the migration velocity. Smith (1995) has studied the thermocapillary migration of a two-dimensional liquid droplet on a non-uniformly heated horizontal plate, where the droplet is thin enough so that lubrication theory can be applied to develop an evolution equation for the shape of the free surface. Ford & Nadim (1994) have established a model for the thermocapillary migration of a thin two-dimensional droplet having an arbitrary height profile on a solid surface. The thermocapillary motion of spherical-cap drops on horizontal glass surfaces coated with poly(dimethylsiloxane) (PDMS) has been reported by Pratap *et al.* (2008), and a theoretical description has also been presented. Dai *et al.* (2016) have carried out experimental and theoretical studies to investigate the migration behaviour of a lubricant droplet induced by a unidirectional thermal gradient. Later, this work was extended to migration induced by an omnidirectional thermal gradient (Dai *et al.* 2018) and on radially microgrooved surfaces (Dai *et al.* 2019).

In thermocapillary migration, convection is induced within the droplet. Once the temperature gradient on the free surface exceeds a threshold, the convection will become unstable. Owing to its crucial importance in many applications, especially in crystal growth (Duffar 2010), the thermocapillary instability has received much attention in the past four decades. The related works have been reviewed by Davis (1987), Schatz & Neitzel (2001) and Lappa (2009).

Smith & Davis (1983*a*) have examined the linear stability of a thermocapillary liquid layer, where an infinite liquid layer on a rigid adiabatic plane is set in motion by imposing a constant temperature gradient on the gas–liquid interface. They found two kinds of instabilities: convective instability (CI) and surface wave instability (SWI). When the free surface is assumed to be non-deformable, CI is dominant, which is driven by mechanisms within the bulk of the layer. In experiments (Riley & Neitzel 1998) and numerical simulations (Li *et al.* 2004), hydrothermal waves of CI have been observed. The mechanism of CI is purely hydrodynamic at small Prandtl numbers (Pr), but hydrothermal at large Pr (Wanschura *et al.* 1995; Yan, Hu & Chen 2018). Chan & Chen (2010) have performed a linear stability analysis of thermocapillary–buoyancy convection in a horizontal fluid layer. The critical parameters they obtained agree with the experimental results reported by Riley & Neitzel (1998).

On the other hand, when surface deformation is considered, SWI can occur. Smith & Davis (1983*b*) have investigated the two-dimensional mode that couples the interfacial deflection to the base flow. It has been found that SWI is most prominent at low Pr and

is hydrodynamic in nature (Davis 1987). Later, Patne, Agnon & Oron (2020, 2021*a*) have generalized this work to three-dimensional disturbances for a liquid layer subjected to an oblique temperature gradient and the case of a viscoelastic fluid (2021*b*).

There are also some experiments on SWI. Duan, Kang & Hu (2006) have performed an experimental study on the surface deformation in thermocapillary convection, which proves that SWI exists on the free surface. Zhu *et al.* (2011) have reported the surface oscillation of thermocapillary convection in a rectangular pool of silicone oil. Bach & Schwabe (2015) have reviewed and complemented the experimental results on SWI in thermocapillary annular gaps, which show that surface waves exhibit a considerably larger frequency, phase speed and surface deformation amplitude compared to hydrothermal waves.

The controllability of a droplet is highly dependent on the stability of the flow during migration. Determining the critical parameters of the transition and instability mechanism will enrich our understanding of droplet dynamics, and guide future development of microfluidics. However, to our best knowledge, few works have been carried out in this field. The only one we know is our previous study on the CI of thermocapillary–buoyancy convection in droplet migration (Hu, Yan & Chen 2019), where hydrothermal waves are detected at critical Marangoni numbers.

In the present work, we would like to pay attention to the SWI of thermocapillary migration. Although SWI in thermocapillary convection is an existing problem, previous works have been confined to a few cases of liquid layers, and experiments reporting SWI are limited. Therefore, the understanding of SWI is very in adequate. The surface deflection cannot tell us directly whether the instability belongs to SWI, as some experiments show that faint surface oscillations can be found in CI and sometimes SWI can coexist with CI (Bach & Schwabe 2015). The properties of and the instability mechanism for SWI need to be clarified. The present work suggests that the kind of instability depends on several parameters besides the capillary number Ca, which measures the surface deflection. In addition, we find new modes and mechanisms that can enrich the understanding of SWI in thermocapillary convection. In many applications of droplet migration, the fluids are polymeric liquids. Thus, both a Newtonian fluid and a viscoelastic fluid are considered in our investigation.

The paper is arranged as follows. In § 2, the problem statement and dimensionless governing equations are introduced. The base-state solution and perturbation equations are derived. After that, critical parameters, perturbation fields and energy mechanisms are presented in § 3. Later, we discuss the instability mechanism and make comparisons with available experiments in § 4. Finally, major conclusions are summarized in § 5.

2. Problem formulation

Referring to figure 1, we consider a thin droplet on a horizontal plane with a temperature gradient in the x direction (Dai *et al.* 2016); y and z are the spanwise and wall-normal directions, respectively. As a simplification, we assume that the droplet is an infinitely long strip in the y direction with width L and thickness d (Ford & Nadim 1994). The liquid is in contact with an inviscid atmosphere. Suppose the surface tension varies linearly with the temperature T:

$$\sigma' = \sigma_0' - \gamma(T - T_0), \tag{2.1}$$

where γ is the surface tension coefficient. Thus, the droplet can be set in motion by the thermocapillary effect.

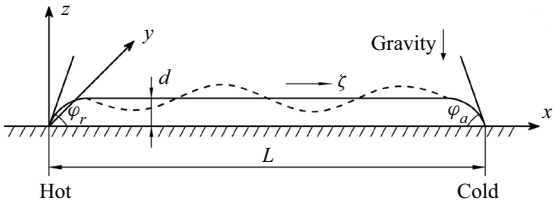

Figure 1. Side view of thermocapillary migration for a thin droplet on a solid plane. The droplet can be susceptible to SWI when its surface is deformable.

In the vicinity of the three-phase contact line, φ_a and φ_r are the advancing and receding contact angles, respectively. Contact angle hysteresis is found in many droplet migrations (Chen *et al.* 2005; Pratap *et al.* 2008). However, Brzoska, Brochard-Wyart & Rondelez (1993) have shown that typical contact angle hysteresis is $\tilde{\delta} = \cos\varphi_a - \cos\varphi_r = 1.5 \times 10^{-2}$ for silicone oils and $\tilde{\delta} = 10^{-2}$ for n-alkanes, while the variations of contact angle with temperature are extremely small. As the difference between φ_a and φ_r is not crucial for the stability analysis, we assume that $\varphi_a = \varphi_r = \varphi$ for simplicity in the following.

Generally, the droplet has an oval shape. However, when L is much larger than the capillary length $\hat{\kappa}^{-1} = \sqrt{\sigma'_0/(\rho_0 g)}$, the droplet can be flattened by gravity and forms a pancake, while the thickness in the base state is a constant $d = 2\hat{\kappa}^{-1}\sin(\varphi/2)$ except in the rim of the droplet (Brochard 1989). Here, σ'_0, ρ_0 and g are the surface tension, fluid density and gravitational acceleration, respectively. This can also be seen in the experiment (figure 2 of Dai *et al.* 2016). Thus, d is assumed to be a constant. In addition, we consider the case when φ is not too small, so that d has the same order as $\hat{\kappa}^{-1}$, and $L \gg d$.

2.1. *Governing equations*

We suppose that the liquid is an incompressible fluid, whose dynamic viscosity μ and thermal diffusivity χ are constants. Both a Newtonian fluid and a viscoelastic fluid are considered in the following. The latter is modelled by an Oldroyd-B fluid, which can be derived from the kinetic theory for a dilute suspension of polymer molecules in a Newtonian solvent (Bird, Armstrong & Hassager 1987).

The dimensionless numbers can be given as follows:

$$Ma = \frac{b\gamma d^2}{\chi\mu}, \quad Pr = \frac{\mu}{\rho\chi}, \quad R = \frac{Ma}{Pr} = \frac{\rho U d}{\mu}, \quad S = \frac{\rho d\sigma'_0}{\mu^2}, \tag{2.2a}$$

$$Ca = \frac{Ma}{PrS}, \quad G = \frac{\rho g d^2}{\mu U}, \quad Bo = \frac{\rho_0 g\kappa d^2}{\gamma}. \tag{2.2b}$$

Here, Ma is the Marangoni number, which measures the thermocapillary effect; b is the temperature gradient on the plane; Pr is the Prandtl number; R is the Reynolds number; S is the non-dimensional surface-tension number; $U = b\gamma d/\mu$ is the velocity scale; and Ca is the capillary number, which measures the magnitude of the surface deformation (Smith & Davis 1983*a*). When S is large enough, $Ca \to 0$ and the surface deformation can be neglected, and CI rather than SWI is preferred. However, when $O(Ca) \geq 0.001$, the surface wave can be the preferred mode in some cases (Smith & Davis 1983*b*). Also above, G is the Galileo number, which measures the gravity effect; and Bo is the dynamic Bond number, which measures the buoyancy effect. Suppose the fluid density varies linearly

Length	Velocity	Stress	Density	Temperature
$d = 2\sqrt{\sigma'_0/\rho_0 g}\sin(\varphi/2)$	$U = b\gamma d/\mu$	$F_0 = \mu U/d$	ρ_0	bd

Table 1. The scales of non-dimensionalization.

ρ(kg m^{-3})	μ(m^2 s^{-1})	γ(N K^{-1} m^{-1})	χ(m^2 s^{-1})	σ'_0 (N m^{-1})	Pr
2.5×10^3	0.88×10^{-3}	4.3×10^{-4}	1.53×10^{-5}	0.72	0.023
φ	b(K mm^{-1})	g(m s^{-2})	$\hat{\kappa}^{-1}$ (mm)	d(mm)	U(m s^{-1})
21°	0.5	9.8	$O(5)$	$O(2)$	$O(0.5)$
R	S	Ca	Ma	G	L(cm)
$O(3 \times 10^3)$	$O(4.6 \times 10^6)$	$O(1 \times 10^{-3})$	$O(6)$	$O(200)$	$O(4)$

Table 2. The values of physical and dimensionless parameters for liquid silicon.

with the temperature,

$$\rho = \rho_0[1 - \kappa(T - T_0)], \tag{2.3}$$

where κ is the thermal expansion coefficient. We can see that Bo is independent of the surface tension gradient. Although the fluid is assumed to be incompressible, the variation of density with temperature in the presence of gravity can lead to a buoyancy effect, which may change the flow significantly. So the Boussinesq approximation is used.

The dimensionless governing equations can be obtained as follows, which are the continuity equation, the momentum equation and the energy equation, respectively (Yan *et al.* 2018); the scales of non-dimensionalization are presented in table 1:

$$\nabla \cdot \boldsymbol{u} = 0, \tag{2.4}$$

$$R\left(\frac{\partial \boldsymbol{u}}{\partial t} + \boldsymbol{u} \cdot \nabla \boldsymbol{u}\right) = -\nabla p + \nabla \cdot \boldsymbol{\tau} + (Bo\,T - G)\nabla z, \tag{2.5}$$

$$\frac{\partial T}{\partial t} + \boldsymbol{u} \cdot \nabla T = \frac{1}{Ma}\nabla^2 T. \tag{2.6}$$

Here, $\boldsymbol{u} = (u, v, w)$, p, T and $\boldsymbol{\tau}$ stand for the velocity, pressure, temperature and stress, respectively. The buoyancy effect is taken into account in the momentum equation (Hu *et al.* 2018). When $G \gg L/d$, we have $\rho g d \gg (\mu U/d^2)L$, which means that the variation of pressure along the x direction is much smaller than the pressure caused by gravity. Thus, the thickness expression $d = 2\hat{\kappa}^{-1}\sin(\varphi/2)$ derived by Brochard (1989) is still valid for droplet migration.

For example, the values of physical and dimensionless parameters for liquid silicon (Smith & Davis 1983*b*) are stated in table 2. Here, we set the values of φ, b and L. It can be seen that the dimensionless parameters Pr, R, S, Ca, Ma and G are within the ranges we will consider in this paper. In addition, $L \gg \hat{\kappa}^{-1}$, d and $G \gg L/d$, while the variation of surface tension along the x direction is small: $bL\gamma \ll \sigma'_0$.

The dimensionless constitutive equation for a Newtonian fluid is

$$\boldsymbol{\tau} = \boldsymbol{S}, \tag{2.7}$$

where $\frac{1}{2}\boldsymbol{S} = \frac{1}{2}[\nabla \boldsymbol{u} + (\nabla \boldsymbol{u})^{\mathrm{T}}]$ is the strain-rate tensor. For an Oldroyd-B fluid, one has

$$\left(1 + \lambda \frac{\delta}{\delta t}\right)\boldsymbol{\tau} = \left(1 + \lambda\tilde{\beta}\frac{\delta}{\delta t}\right)\boldsymbol{S}, \tag{2.8}$$

where $\delta/\delta t$ is the upper convected derivative with the expression

$$\frac{\delta \boldsymbol{\tau}}{\delta t} = \frac{\partial \boldsymbol{\tau}}{\partial t} + \boldsymbol{u}\cdot\nabla\boldsymbol{\tau} - (\nabla\boldsymbol{u})^{\mathrm{T}}\cdot\boldsymbol{\tau} - \boldsymbol{\tau}\cdot(\nabla\boldsymbol{u}). \tag{2.9}$$

Here, $\lambda = (\mu/\tilde{G})(U/d)$ is the Weissenberg number, $\tilde{G}$ is the elastic modulus and $\tilde{\beta}$ is the ratio of solvent viscosity to total viscosity. The elasticity number $\varepsilon = \lambda/R$ is used in the following, as it depends only on the properties of the fluid and the geometry. When $\lambda = 0$ or $\tilde{\beta} = 1$, the Oldroyd-B fluid recovers the Newtonian fluid.

We choose the reference frame travelling with the droplet, while the plane moves at the speed of ζ in the negative x direction. Thus, the flux in the x direction is zero: $\int_0^1 u\,\mathrm{d}z = 0$. The boundary conditions on the rigid plane are

$$u|_{z=0} = -\zeta, \quad T|_{z=0} = -x, \tag{2.10a,b}$$

where ζ is the dimensionless migration velocity and a temperature gradient is imposed on the plane. We suppose that a deformable gas–liquid interface is located at $z = 1 + \xi(x, y, t)$, where $\xi(x, y, t)$ is the small displacement of the interface from its undisturbed position $z = 1$. The boundary conditions at the interface are presented as follows, which are the kinematic boundary condition, the tangential and normal components of the stress balance (Pérez-García & Carneiro 1991) and the continuity of heat flux, respectively:

$$\partial_t\xi + \boldsymbol{u}_\perp\cdot\nabla\xi = w, \tag{2.11a}$$

$$\boldsymbol{t}_j\cdot\boldsymbol{\tau}\cdot\boldsymbol{n} = -\nabla T\cdot\boldsymbol{t}_j, \tag{2.11b}$$

$$-p + \boldsymbol{n}\cdot\boldsymbol{\tau}\cdot\boldsymbol{n} = -Ca^{-1}(\nabla_s\cdot\boldsymbol{n}) - G\xi, \tag{2.11c}$$

$$-\nabla T\cdot\boldsymbol{n} = 0. \tag{2.11d}$$

In (2.11a), $\boldsymbol{u}_\perp = (u, v)$ is the two-dimensional velocity in the x–y plane; (2.11b) stands for the shear stress caused by the thermocapillary effect; and $\boldsymbol{t}_j$ and $\boldsymbol{n}$ are the unit tangent and unit normal vectors to the free surface, respectively. Their linearized expressions in the perturbed state are (Patne *et al.* 2021*a*)

$$\boldsymbol{n} = -\partial_x\xi\boldsymbol{e}_x + \boldsymbol{e}_z - \partial_y\xi\boldsymbol{e}_y, \quad \boldsymbol{t}_1 = \boldsymbol{e}_x + \partial_x\xi\boldsymbol{e}_z, \quad \boldsymbol{t}_2 = \partial_y\xi\boldsymbol{e}_z + \boldsymbol{e}_y. \tag{2.12a–c}$$

In (2.11c), $\nabla_s = (\boldsymbol{I} - \boldsymbol{nn})\cdot\nabla$ is the surface gradient operator; and finally (2.11d) stands for zero heat flux.

We restrict our attention to flow that is not near the rim of the droplet. Thus, the basic flow is assumed to be parallel, while the temperature is linear in x plus a distribution in z

as follows:

$$\boldsymbol{u} = (U_0(z), 0, 0), \quad T_0(x, z) = -x + T_b(z). \tag{2.13a,b}$$

The velocity and temperature distributions for the base state can be determined as follows (Hu *et al.* 2019):

$$U_0(z) = -\zeta\left(1 - 3z + \frac{3}{2}z^2\right) + \left(-\frac{1}{2}z + \frac{3}{4}z^2\right) + \frac{Bo}{4}\left(-\frac{1}{2}z + \frac{5}{4}z^2 - \frac{2}{3}z^3\right), \tag{2.14a}$$

$$T_b(z) = z^2 Ma\left[\frac{\zeta}{8}(-2+z)^2 + \frac{z}{4}\left(\frac{1}{3} - \frac{1}{4}z\right) + \frac{Bo}{24}\left(\frac{1}{2}z - \frac{5}{8}z^2 + \frac{1}{5}z^3\right)\right]. \tag{2.14b}$$

It is found that the average of the velocity gradient and the surface temperature increase with Bo and ζ, while the upper surface is hotter than the bottom.

When $Bo = 0$, the velocity distribution (2.14*a*) agrees with equation (8) of Pratap *et al.* (2008). The above solutions are the same for the Newtonian fluid and the Oldroyd-B fluid. However, due to the elasticity, there is a normal stress component for the latter. The total stress tensor accounting for both Newtonian and elastic contributions can be given as follows:

$$\boldsymbol{\tau}_0 = \begin{bmatrix} \bar{\tau}_{11} & 0 & \bar{\tau}_{13} \\ 0 & 0 & 0 \\ \bar{\tau}_{13} & 0 & 0 \end{bmatrix}, \tag{2.15}$$

where $\bar{\tau}_{13} = \mathrm{D}U_0(z)$ and $\bar{\tau}_{11} = 2\lambda(1-\tilde{\beta})[\mathrm{D}U_0(z)]^2$ with $\mathrm{D}U_0(z) = (\mathrm{d}/\mathrm{d}z)U_0(z)$.

The migration velocity can be derived as follows:

$$\zeta = \frac{2\cos\phi + 1}{6} + \frac{1}{24}Bo, \tag{2.16}$$

where the details can be found in Hu *et al.* (2019) and Dai *et al.* (2016).

2.2. *Perturbed state*

Now we apply an infinitesimal three-dimensional disturbance in the normal mode form to the base state:

$$(\boldsymbol{u}, T, P, \boldsymbol{\tau}, z) = (\boldsymbol{u}_0, T_0, P_0, \boldsymbol{\tau}_0, 1) + \boldsymbol{\delta}, \tag{2.17a}$$

$$\boldsymbol{\delta} = (\widehat{u}, \widehat{v}, \widehat{w}, \widehat{T}, \widehat{P}, \widehat{\boldsymbol{\tau}}, \widehat{\xi})\exp[\sigma t + \mathrm{i}(\alpha x + \beta y)], \tag{2.17b}$$

where the subscript 0 stands for the basic flow while the variables without subscript 0 refer to the perturbation. The complex eigenvalue $\sigma = \sigma_r + \mathrm{i}\sigma_i$ consists of the growth rate σ_r and the frequency σ_i. The parameters α and β are the wavenumbers in the x and y directions, respectively. The total wavenumber, wave speed and wave propagation angle are defined as $k = \sqrt{\alpha^2 + \beta^2}$, $c = |\sigma_i|/k$ and $\theta = \tan^{-1}(\beta/\alpha)$, respectively. Owing to the symmetry, we only need to consider the case $\theta \in [0^\circ, 180^\circ)$. The perturbation equations have been presented in Hu *et al.* (2018) and the boundary conditions are described in the Appendix.

The Chebyshev collocation method (Schmid & Henningson 2001) is used to solve the general eigenvalue problem in the form of $\boldsymbol{W}\boldsymbol{g} = \sigma\boldsymbol{Z}\boldsymbol{g}$, where $\boldsymbol{W}$ and $\boldsymbol{Z}$ are two matrices, and $\boldsymbol{g}$ is the eigenvector. We set N_c Gauss–Lobatto points for the governing equations in the flow region $z = [1 - \cos(j\pi/(N_c+1))]/2$, $j = 1 - N_c$, and two points for the boundary conditions at $z = 0,1$ (2.25). The results are sufficiently accurate when $N_c = 80 - 100$.

(*a*) Linear flow								(*b*) Return flow			
Pr	*S*	*R*		*k*		*c*		*Pr*	*k*	*R*	
		SD	PW	SD	PW	SD	PW			SD	PW
0	10^4	324.2	343.42	1.91	1.87	0.2825	0.3009	0	0.2	19.3	19.69
1	10^4	331.5	348.77	1.84	1.82	0.2905	0.3058	0.015	0.2	28.1	29.08
0	10^5	858.8	875.3	1.87	1.83	0.2057	0.2138	0.1	0.2	200.2	206.3
1	10^5	876.2	890.32	1.76	1.74	0.2151	0.2212	1	0.4	120.8	127.82

Table 3. Some parameters of the two-dimensional SWI in thermocapillary liquid layers: (*a*) critical parameters of the linear flow; and (*b*) neutral Reynolds numbers of the return flow. Here, 'SD' and 'PW' stand for the results of Smith & Davis (1983*b*) and the present work, respectively.

Parameter	Experiment	Linear stability analysis	
	RN	CC	PW
Ma	366	343.3	343.6
θ	23.2°	21.7°	21.9°
k	2.58	2.48	2.47
σ_i	0.0217	0.0237	0.0234
c	0.0561	0.0583	0.0579

Table 4. The critical parameters of CI in the thermocapillary–buoyancy convection at $Pr = 13.9$ and $Bo = 0.142$. Here, 'RN', 'CC' and 'PW' stand for the results of Riley & Neitzel (1998), Chan & Chen (2010) and the present work, respectively.

ε	*R*	α	ω
0.0001	5167	1.05	0.287
0.0005	4058	1.13	0.332
0.0010	3925	1.14	0.334

Table 5. The critical parameters of plane Poiseuille flow for the Oldroyd-B fluid ($\tilde{\beta} = 0.5$, $\beta = 0$). Our results are exactly the same as those in Sureshkumar & Beris (1995).

In order to validate our code, we compute some parameters of the two-dimensional SWI in the thermocapillary liquid layer in table 3 and the critical parameters of CI in the thermocapillary–buoyancy convection in table 4. The code for the constitutive equations of an Oldroyd-B fluid is validated by computing the critical parameters of plane Poiseuille flow for the Oldroyd-B fluid in table 5. Most of perturbation equations in the liquid layer and the channel flow are the same as those in the droplet migration, so we only need to change the basic flow and some boundary conditions in the code. Comparisons are made with the results of Smith & Davis (1983*b*), Riley & Neitzel (1998), Chan & Chen (2010) and Sureshkumar & Beris (1995). Our results are comparable to those in the previous works.

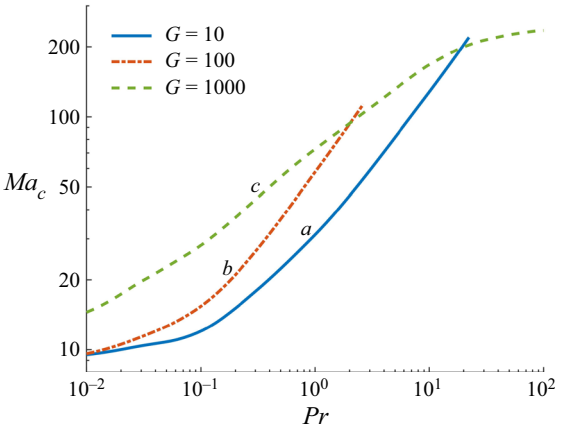

Figure 2. The variation of Ma_c with Pr at $\zeta = 0.49$, $Ca = 0.001$ and $Bo = 0$. The curves correspond to streamwise waves of SWI (a and b) and the oblique wave of CI (c).

3. Numerical results

We determine the neutral Marangoni numbers Ma_N of neutral modes ($\sigma_r = 0$). Then, the critical Marangoni number Ma_c can be obtained, which is the global minimum of Ma_N for all (α, β):

$$Ma_c = \min_{\alpha,\beta} Ma_N(\zeta, Pr, G, Ca, Bo, \varepsilon). \tag{3.1}$$

The flow is linearly stable for any modes when $Ma < Ma_c$.

The computation suggests that there are two kinds of instability: CI and SWI. The former has been examined in our previous work (Hu *et al.* 2019). For the latter, two kinds of preferred modes are detected, which are the streamwise wave ($\theta = 0^\circ$ or 180°) and the oblique wave ($\theta \neq 0^\circ$, 90° and 180°). The results for the Newtonian fluid and for the Oldroyd-B fluid are presented in §§ 3.1 and 3.2, respectively.

3.1. *Newtonian fluid*

3.1.1. *The effect of the Galileo number*

First, we study the effect of the Galileo number G on the instability. The variation of Ma_c with Pr at $\zeta = 0.49$, $Ca = 0.001$ and $Bo = 0$ is displayed in figure 2. It can be seen that Ma_c always increases with Pr. SWI is preferred at $Pr < 19.1$ for $G = 10$ and $Pr < 2.05$ for $G = 100$. The preferred mode is the downstream streamwise wave ($\theta = 0^\circ$, curves a and b in figure 2), and Ma_c increases with G. When Pr becomes larger, the preferred mode changes to the oblique wave of CI (curve c in figure 2), which is independent of G. When $G = 1000$, we can only find CI in the flow.

In figure 3, we show the wavenumber, propagation angle and wave speed of the preferred modes. It can be seen that, for SWI, the wavenumbers are less than 0.6. The wave speeds increase significantly with Pr. For CI, the wavenumbers are of the order of 2, the oblique wave travels upstream ($90^\circ < \theta < 180^\circ$) and the wave speed is much smaller than those of SWI. We will confine ourselves to the case of $G = 100$ in the following study.

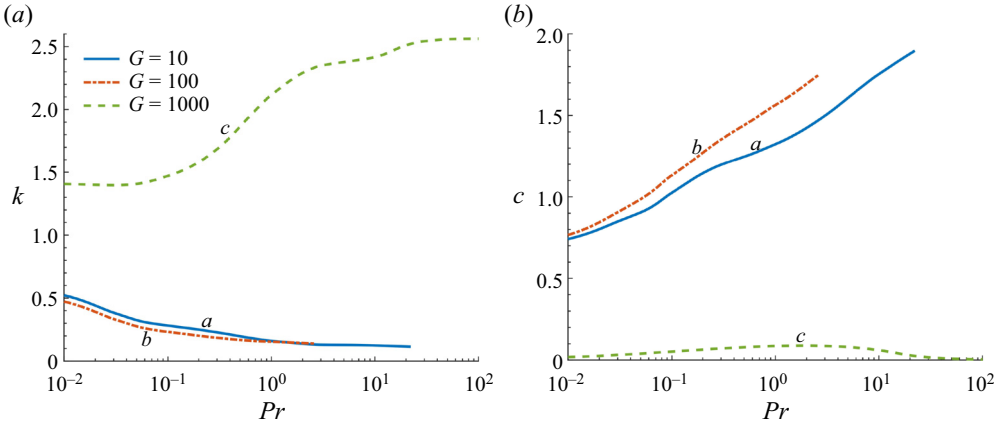

Figure 3. The (*a*) wavenumber and (*b*) wave speed of the modes in figure 2.

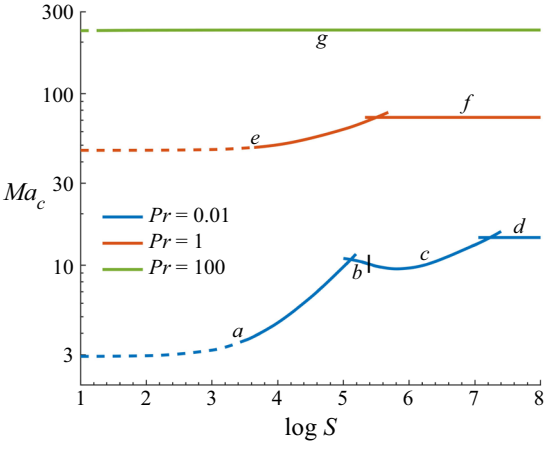

Figure 4. The variation of Ma_c with S at $\zeta = 0.49$ and $Bo = 0$. The curves correspond to streamwise waves (*a*, *c* and *e*) and oblique waves (*b*, *d*,*f* and *g*). SWI includes curves *a*, *b*, *c* and *e*, while CI includes curves *d*,*f* and *g*. The dashed portions of curves *a*, *e* and *g* are where the condition (A3) is not satisfied.

3.1.2. *The effect of the surface-tension number*

In this section, we study the effect of the surface-tension number S. The variation of Ma_c with S is displayed in figure 4. The dashed portions of curves *a* and *e* are where the condition (A3) is not satisfied. When $Pr = 0.01$, the preferred mode includes the streamwise waves (curves *a* and *c* in figure 4) and the oblique waves (curves *b* and *d* in figure 4). Here, curve *b* belongs to the SWI whose propagation angle has $\theta \in (0^\circ, 40^\circ)$. When S is large enough, the preferred mode changes from SWI to CI. When $Pr = 1$, the SWI is more prominent at $S < 3.39 \times 10^5$ (curve *e* in figure 4). When $Pr = 100$, only the CI is found. There are two kinds of streamwise waves, which travel upstream ($\theta = 180^\circ$, curve *a*) and downstream ($\theta = 0^\circ$, curves *c* and *e*), respectively.

The wavenumber and wave speed of the preferred modes are displayed in figure 5. In the following, we will confine ourselves to the case $Ca = R/S = 0.001$, so that the condition (A3) can always be satisfied.

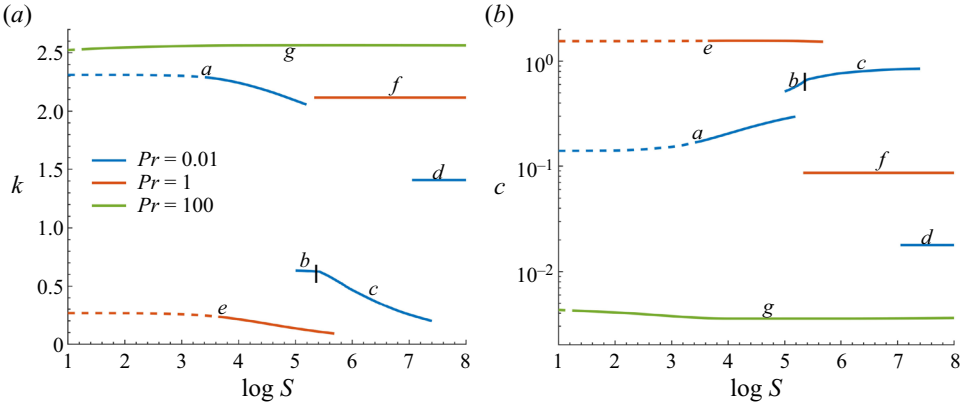

Figure 5. The (*a*) wavenumber and (*b*) wave speed of the modes in figure 4.

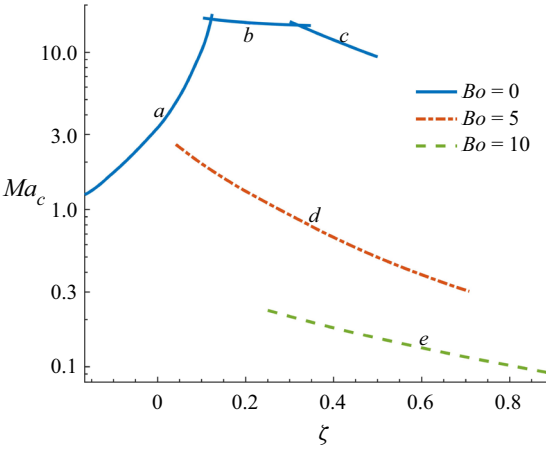

Figure 6. The variation of Ma_c with ζ and Bo at $Pr = 0.01$. The curves correspond to streamwise waves of SWI (*a*, *c*, *d* and *e*) and the oblique wave of CI (*b*).

3.1.3. *The effects of the migration velocity and the Bond number*

The effects of the migration velocity ζ and the Bond number Bo are discussed in this section.

(A) $Pr = 0.01$

The variations of Ma_c with ζ and Bo at $Pr = 0.01$ are displayed in figure 6. It can be seen from (2.16) that the region of ζ depends on Bo. The Ma_c value always decreases with Bo. When $Bo = 0$, the variation of Ma_c with ζ is non-monotonic. The preferred modes include the streamwise waves of SWI (curves *a* and *c* in figure 6) and the oblique wave of CI (curve *b* in figure 6). Here, curves *a* and *b* correspond to the wave travelling upstream ($\theta > 90°$) while curve *c* corresponds to the wave travelling downstream ($\theta < 90°$). When $Bo = 5$ and 10, Ma_c always decreases with ζ. The preferred modes are the downstream streamwise waves of SWI (curves *d* and *e* in figure 6).

The wavenumber and wave speed of the preferred modes in figure 6 are displayed in figure 7. It can be seen that the wavenumbers of SWI (curves *a*, *c*, *d* and *e* in figure 7) are

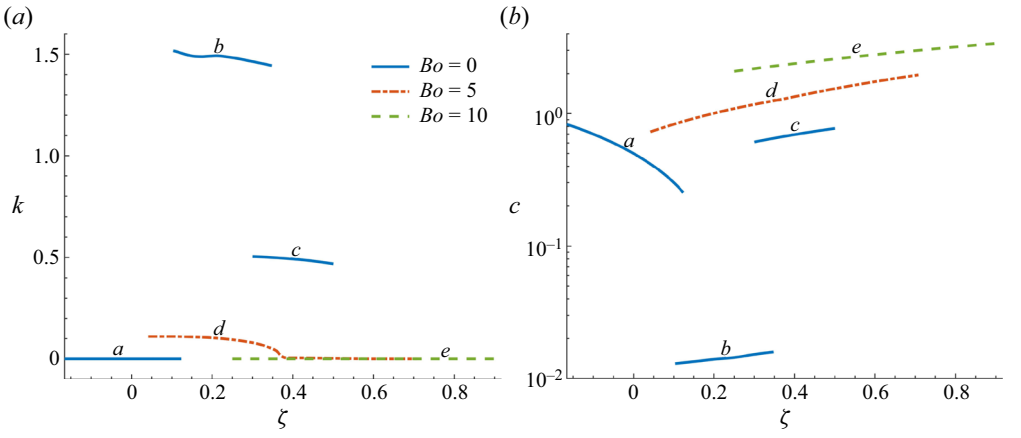

Figure 7. The (*a*) wavenumber and (*b*) wave speed of the modes in figure 6.

much smaller than those of CI (curve *b* in figure 7), while the reverse is true for the wave speed.

The wavenumbers of curves *a*, *d* and *e* in figure 7 tend to zero, which means that they belong to the long-wave instability. For these modes, Ma_N increases with k. However, the wavenumber of SWI cannot be arbitrarily small. Owing to (A3), $k \gg Ca \times 2\pi \approx 0.006$. In addition, the largest wavelength is the width L, which leads to $k \geq 2\pi d/L$. Therefore, the actual Ma_c will be larger than the value shown in figure 6. When $Bo = 0$ and $\zeta = 0$, the Ma_c of CI is 19.38. Thus, SWI is preferred when $k < 0.094$. If this value does not satisfy the previous requirements, CI will be preferred.

Here, the perturbation flow fields of the preferred modes at $Pr = 0.01$ are plotted in figure 8. It can be seen that there are hot spots on the surface. In figure 8(*a*) (respectively, figure 8*b*,*c*), the vertical up-flow on the surface at the phase $\phi = 3.5$ make ξ increase, so the wave travels upstream (respectively, downstream), while the hot spot is near the wave trough (respectively, crest). There is no roll in the flow field, which is different from the case of CI. The modes in figures 8(*a*) and 8(*b*) belong to the long-wave instability.

(B) $Pr = 1$

Figure 9 shows Ma_c at $Pr = 1$. The variation of Ma_c with Bo is non-monotonic; and Ma_c decreases with ζ except for the case at $Bo = 0$, $\zeta < -0.025$. The preferred modes include the streamwise waves of SWI (curves *a*, *c*, *e* and *f* in figure 9) and the oblique waves of CI (curves *b* and *d* in figure 9). Here, curves *a*, *b* and *d* travel upstream, while curves *c*, *e* and *f* travel downstream.

The wavenumber and wave speed of the preferred modes in figure 9 are displayed in figure 10. Here, curves *a*, *e* and *f* in figure 10 belong to the long-wave instability. Once again, the wavenumbers (wave speeds) of SWI are much smaller (larger) than those of the CI.

(C) $Pr = 100$

The variations of Ma_c with ζ and Bo at $Pr = 100$ are displayed in figure 11. The preferred modes include the streamwise waves of SWI (curves *a*, *c* and *d* in figure 11) and the oblique wave of CI (curve *b* in figure 11). Here, curves *a* and *b* travel upstream, while curves *c* and *d* travel downstream. SWI is dominant at $Bo > 0$.

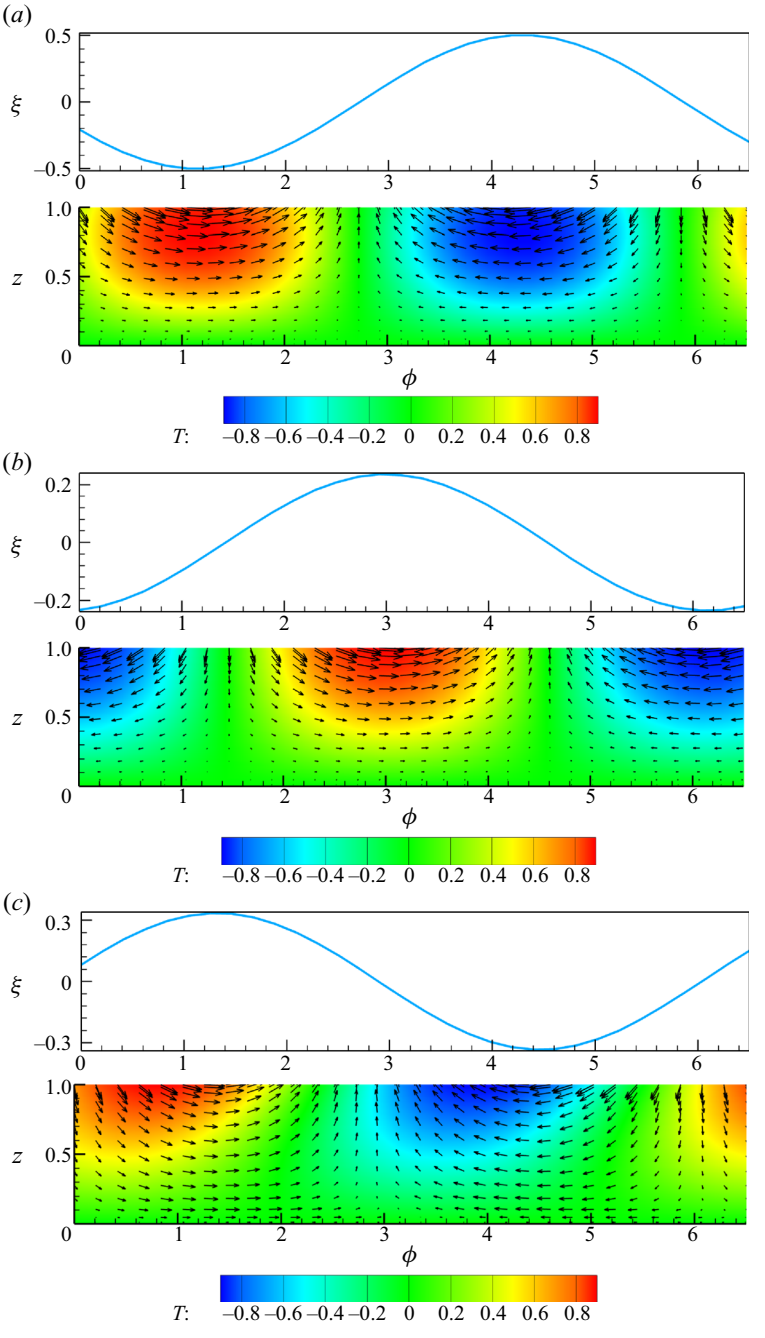

Figure 8. The perturbation flow field and surface deformation at $Pr = 0.01$, $Ca = 0.001$ and $G = 100$: (*a*) $Bo = 0$, $\zeta = 0$; (*b*) $Bo = 10$, $\zeta = 0.5$; and (*c*) $Bo = 0$, $\zeta = 0.49$. The perturbation phase is defined as $\phi = \alpha x + \beta y$.

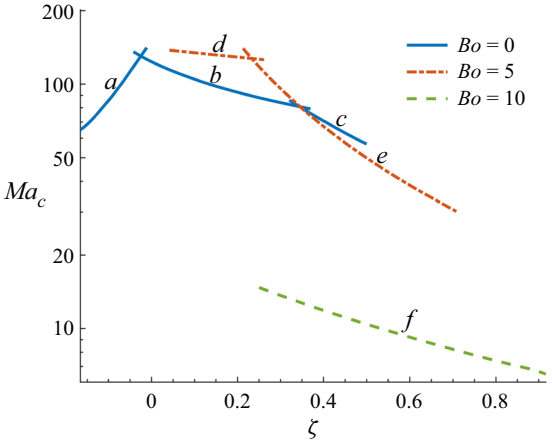

Figure 9. The variation of Ma_c with ζ and Bo at $Pr = 1$. The curves correspond to streamwise waves of SWI (a, c, e and f) and oblique waves of CI (b and d).

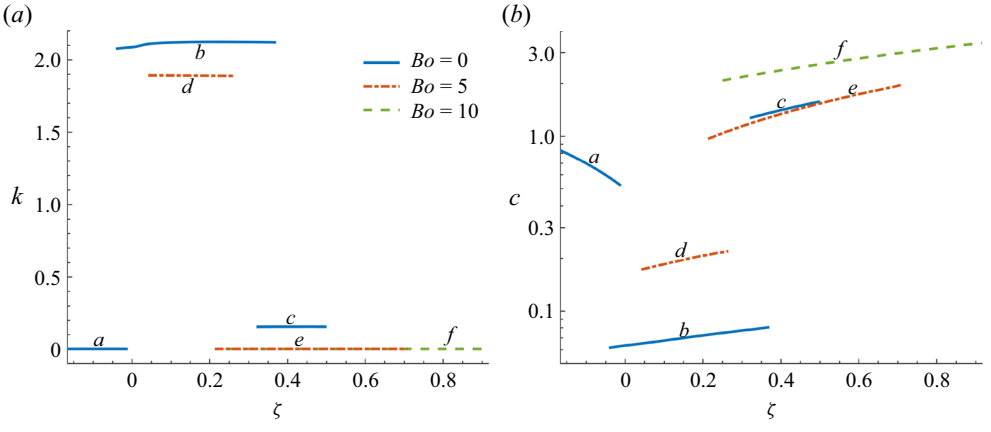

Figure 10. The (a) wavenumber and (b) wave speed of the modes in figure 9.

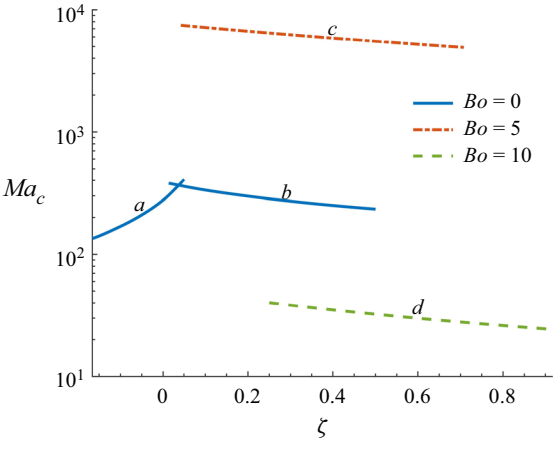

Figure 11. The variation of Ma_c with ζ and Bo at $Pr = 100$. The curves correspond to streamwise waves of SWI (a, c and d) and the oblique wave of CI (b).

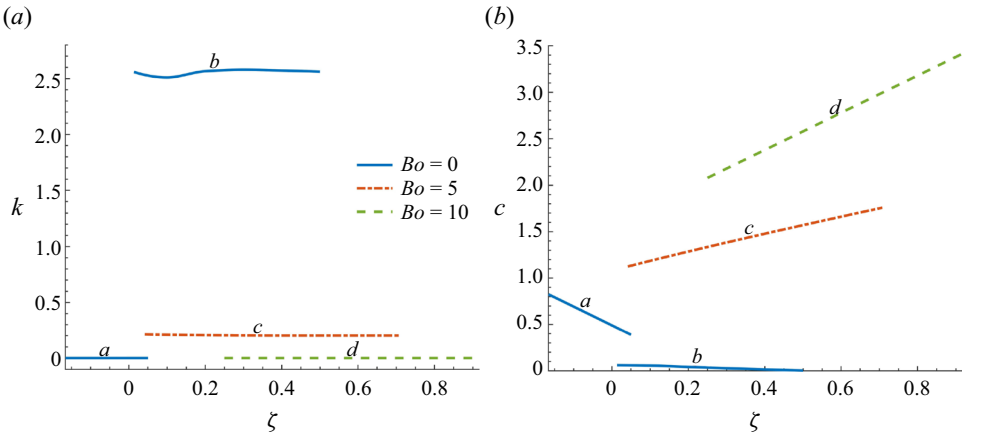

Figure 12. The (*a*) wavenumber and (*b*) wave speed of the modes in figure 11.

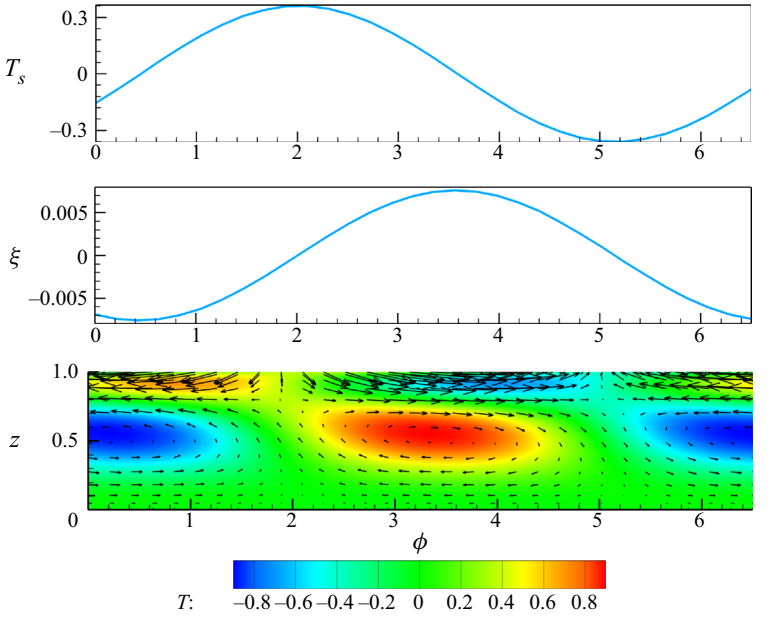

Figure 13. The perturbation flow field and surface deformation at $Pr = 100$, $\zeta = 0.4$, $Bo = 5$, $Ca = 0.001$ and $G = 100$. The preferred mode is the downstream streamwise wave. Here, T_s is the perturbation temperature on the surface.

The wavenumber and wave speed of the preferred modes in figure 11 are displayed in figure 12. Here, curves *a* and *d* in figure 12 belong to the long-wave instability. For SWI, the wave speed increases with ζ when $Bo > 0$. The relationship between SWI and CI is similar to the cases at $Pr = 0.01$ and 1.

When $Bo > 0$, there is a new type of perturbation field, which is displayed in figure 13. We can find two hot spots in the vertical direction ($z = 0.5$ and 0.9). There are two rolls in one cycle ($\phi \in [0, 2\pi]$), which almost coincide with the isothermals.

3.1.4. *Energy analysis*

The energy mechanism of SWI is studied in this section. The rate of change for the perturbation energy can be derived as follows (Wanschura *et al.* 1995; Hu, Peng & Zhu 2012):

$$\begin{aligned}\frac{\partial E_{kin}}{\partial t} &= -\frac{1}{R}\int p\boldsymbol{u}\cdot\boldsymbol{n}\,\mathrm{d}^2r - \frac{1}{2R}\int(\boldsymbol{\tau}:\boldsymbol{S})\,\mathrm{d}^3r + \frac{1}{R}\int \boldsymbol{u}\cdot\boldsymbol{\tau}\cdot\boldsymbol{n}\,\mathrm{d}^2r \\ &\quad - \int \boldsymbol{u}\cdot[(\boldsymbol{u}\cdot\nabla)\boldsymbol{u}_0]\,\mathrm{d}^3r + \int\left(\frac{Bo}{R}T\boldsymbol{e}_3\cdot\boldsymbol{u}\right)\mathrm{d}^3r \\ &= P - N + M + I + B. \end{aligned} \tag{3.2}$$

Here, P is the work done by the pressure on the surface, N is the work done by stress in the bulk of the layer, M is the work done by stress on the surface, I is the energy from the basic flow, and B is the work done by the buoyancy (Hu *et al.* 2018); and $\int f\,\mathrm{d}^2r$ and $\int f\,\mathrm{d}^3r$ stand for the surface and volume integrals, respectively. For the Newtonian fluid, $\boldsymbol{\tau}=\boldsymbol{S}$, so $N>0$, which stands for the viscous dissipation. The perturbation is normalized as $\int|\boldsymbol{u}|^2\,\mathrm{d}^3r=1$.

As the stress on the deformed surface has horizontal and vertical components, M can be decomposed into two terms as follows:

$$M = \frac{1}{R}\int(u\tau_{13}+v\tau_{23})\,\mathrm{d}^2r + \frac{1}{R}\int w\tau_{33}\,\mathrm{d}^2r = M_h + M_v. \tag{3.3}$$

In addition, we can see from (A2*b*) and (A2*c*) that shear stress can be induced by the Marangoni effect and the surface deformation. Thus, M_h is decomposed into the following two terms:

$$M_h = M_{h,T} + M_{h,\xi}, \tag{3.4}$$

$$M_{h,T} = \frac{1}{R}\int\left[u\left(-\frac{\partial T}{\partial x}\right)+v\left(-\frac{\partial T}{\partial x}\right)\right]\mathrm{d}^2r, \tag{3.5}$$

$$M_{h,\xi} = \frac{1}{R}\int\left[u(-\partial_z T_0+\bar{\tau}_{11})\frac{\partial\xi}{\partial x} - u\frac{\partial\bar{\tau}_{13}}{\partial z}\xi + v(-\partial_z T_0)\frac{\partial\xi}{\partial y}\right]\mathrm{d}^2r. \tag{3.6}$$

Table 6 shows the terms of perturbation energy growth for SWI. It can be seen that M is often the main energy source, I is important in some cases at small Pr, while B is negligible; P always leads to dissipation. The maximum of $|P/N|$ is 12 %, while $|P/N|<3$ % in most cases, so P is not essential for the energy mechanism. Also, M_h is much larger than M_v. For the long-wave mode (cases 1 and 5), M_h is caused by the surface deformation, while for the mode with finite wavelength (cases 2, 3 and 4), it is caused by the Marangoni effect.

3.2. *Oldroyd-B fluid*

We study the effect of elasticity in this section. The variation of Ma_c with ε at $\zeta=0.49$, $Bo=0$ and $\tilde{\beta}=0.1$ is displayed in figure 14. The choice of $\zeta=0.49$ is close to the complete wetting case $\zeta=0.5$ (equivalently $\varphi=0^\circ$). The downstream streamwise wave of SWI is preferred at small ε (curves *a*, *d* and *f* in figure 14). We can see that Ma_c increases slightly with ε at $Bo=0$, while the reverse is true for $Bo>0$. When ε is large enough, the preferred mode changes to the waves of CI (curves *c*, *e* and *g* in figure 14),

Case	1	2	3	4	5
P	0	−0.002191	−0.001369	−0.001684	−0.000072
$-N$	−0.009092	−0.018240	−0.049041	−0.298199	−10.05617
$M_{h,\xi}$	0.009094	−0.000160	−0.008890	0.030112	10.057829
$M_{h,T}$	0	0.006561	0.045132	0.274575	0.020422
M_v	0	0.000647	0.000842	0.001442	0.000040
I	−0.000002	0.013383	0.013327	0.009323	−0.000013
B	0	0	0	−0.015569	−0.022012

Table 6. The terms of the perturbation energy growth for SWI: case 1, $Pr = 0.01$, $Bo = 0$, $\zeta = 0$; case 2, $Pr = 0.01$, $Bo = 0$, $\zeta = 0.49$; case 3, $Pr = 1$, $Bo = 0$, $\zeta = 0.35$; case 4, $Pr = 100$, $Bo = 5$, $\zeta = 0.4$; and case 5, $Pr = 100$, $Bo = 10$, $\zeta = 0.6$.

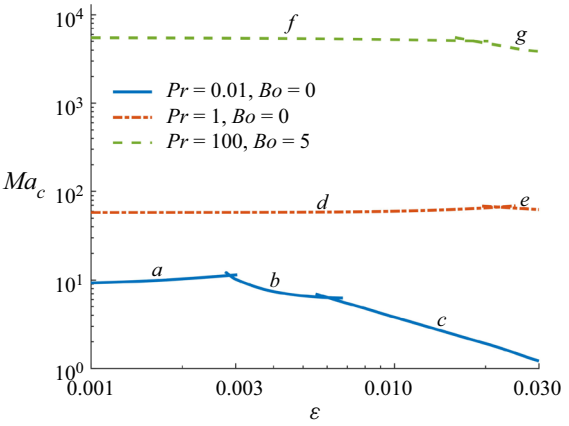

Figure 14. The variation of Ma_c with ε at $\zeta = 0.49$, $Bo = 0$ and $\tilde{\beta} = 0.1$. The curves correspond to downstream streamwise waves (a, b, c, d and f) and upstream oblique waves (e and g). SWI includes curves a, b, d and f, while CI includes curves c, e and g.

while Ma_c decreases with ε. For SWI, the perturbation flow field and energy mechanism of the Oldroyd-B fluid are similar to those of the Newtonian fluid.

4. Discussion

In this section, we compare the properties of SWI and CI. The differences between the droplet and liquid layers are demonstrated. The instability mechanism of SWI is discussed and comparisons are made with experimental results.

4.1. *Comparison of SWI and CI*

First, we compare SWI with CI in thermocapillary migration. For SWI, the most preferred modes are streamwise waves. The only oblique wave of SWI is found at small Pr in figure 4. On the contrary, the most preferred modes of CI are oblique waves, while the streamwise wave of CI appears at high Pr (Hu *et al.* 2019). In the energy mechanism, the work done by buoyancy is always negative in SWI, while that of CI is positive. For small Pr, I is dominant in CI, while I is less important in SWI. The wavenumbers and wave speeds of SWI and CI will be discussed later.

4.2. *Comparison of droplet migration and liquid layers*

Next, we compare the droplet migration with liquid layers. SWI in thermocapillary liquid layers has been examined by Smith & Davis (1983*b*). The basic flow of droplet migration is similar to that of return flow. However, there are many differences between them.

Firstly, in Smith & Davis (1983*b*), SWI is prominent at small Pr and the preferred mode is the two-dimensional streamwise wave ($v = 0$). On the contrary, SWI in droplet migration is detected at $Pr = 0.01 - 100$, while the preferred modes include the two-dimensional streamwise wave and the oblique wave.

Secondly, the energy mechanism of SWI in the liquid layer depends on the flow. For linear flow, the perturbation receives energy from the basic flow through the Reynolds stress and the normal stress on the surface, while for the return flow, the work done by the tangential stress on the surface is dominant in the energy mechanism of long-wave modes. However, in droplet migration, the energy mechanism of SWI depends on the parameters (Pr, ζ and Bo) and modes. Thus, I, $M_{h,\xi}$ and $M_{h,T}$ can be the main energy source in the different cases.

Finally, SWI in the liquid layer is directly related to the isothermal layer subjected to wind stress, and the only role of the temperature field is to drive the basic flow. In droplet migration, the perturbation temperature seems unimportant for the long-wave mode. However, Pr is crucial in the energy mechanism for the mode with finite wavelength, which suggests that the temperature field is very important for SWI.

Patne *et al.* (2021*a*) have considered the thermocapillary instability in a liquid layer with a deformable surface. The layer is heated from below and subjected to an oblique temperature gradient (TG). The instability is induced by this vertical TG but suppressed by a horizontal TG. This is totally different from the case of droplet migration, where the upper surface is hotter than the bottom. The energy analysis shows that the work done by the pressure on the surface (P) is positive for the perturbation growth in Patne *et al.* (2021*a*), while P is negative in the present work.

For the viscoelastic fluid, figure 14 shows that, when $Bo = 0$, weak elasticity can suppress SWI, while strong elasticity changes SWI to CI and destabilizes the flow. The relationship between elasticity and instability is similar to those in a liquid layer with a non-deformable surface (Hu, He & Chen 2016) and in a layer subjected to an oblique TG (Patne *et al.* 2021*a*).

Some preferred modes in figures 7–12 belong to the long-wave instability, whose wave speed, flow field and energy mechanism are independent of Pr. These modes are also found by Smith & Davis (1983*b*) and Patne *et al.* (2021*a*). However, the long-wave mode in the present work can travel either upstream or downstream, while only the upstream wave of the long-wave mode is found by Smith & Davis (1983*b*).

4.3. *Instability mechanism*

The long-wave modes in figures 8(*a*) and 8(*b*) travel upstream and downstream, respectively. Their mechanisms can be explained as follows. As $\alpha \to 0$, it can be seen from (A2*b*) that $\tau_{13} \approx -(\partial \bar{\tau}_{13}/\partial z)\xi$. We can derive the following equation from (2.15):

$$\frac{\partial \bar{\tau}_{13}}{\partial z} = \frac{\mathrm{d}^2}{\mathrm{d}z^2} U_0 = -3\zeta + \frac{3}{2} + \frac{Bo}{4}\left(\frac{5}{2} - 4z\right). \tag{3.7}$$

In figure 8(*a*), $\tau_{13} \approx -\frac{3}{2}\xi$. It can be seen that $u < 0$ near the crest of the surface wave. The key to the mechanism is the proper phasing between the surface deformation ξ and

the horizontal velocity u, so that the perturbation can extract energy from the shear stress on the surface. In figure 8(b), $\tau_{13} \approx \frac{15}{4}\xi$ and $u > 0$ near the crest of the surface wave, which are both opposite to the case in figure 8(a). Its perturbation energy also comes from the work done by shear stress induced by the surface deformation. Therefore, we find that the instability mechanism of the long-wave mode is irrelevant to the Marangoni effect and closely related to the surface deformation. This is the reason why we cannot find these long-wave modes in CI (Hu *et al.* 2019).

In figure 8(c), $\partial\bar{\tau}_{13}/\partial z = 0.03 \ll 1$, so that $M_{h,\xi}$ is negligible. When a horizontal perturbation velocity ($u > 0$) is applied in some place on the surface, the horizontal convection heating $u(\partial T_0/\partial x)$ increases its temperature as $\partial T_0/\partial x|_{z=1} = -1$, and another convection term $U_0(\partial T/\partial x)$ makes the temperature perturbation travel downstream. Meanwhile, due to the continuity equation, there is a small displacement ξ in the vertical direction for the hot spot. However, the Marangoni forces and the pressure near the hot spot induce a restoring force. Owing to the inertia of the fluid, the oscillation of the surface continues. Most of the perturbation energy comes from the basic flow.

In figure 13, the temperature perturbation on the surface is caused by the horizontal convection $u(\partial T_0/\partial x)$ and $U_0(\partial T/\partial x)$. The Marangoni forces near the hot spot at $\phi = 2$ decrease ξ. Then, $u(\partial T_0/\partial x)$ induced by the down-flow and $U_0(\partial T/\partial x)$ make the surface wave travel downstream. The work done by Marangoni forces is the main energy source for the perturbation, while I is less important.

4.4. *Comparisons with thermocapillary instabilities in annular gaps*

Bach & Schwabe (2015) have reported the experiments of thermocapillary instabilities in annular gaps for ethanol. The relevant physical properties are $\rho = 789.4$ kg m^{-3}, $\nu = 1.52 \times 10^{-6}$ m^2 s^{-1}, $\gamma = 9 \times 10^{-5}$ N K^{-1} m^{-1}, $\sigma_0' = 22.75$ N m^{-1}, $d = 1$ mm, $Pr = 17$ and $S = 4.73 \times 10^3$. The velocity scale is $U = b\gamma d/\mu = 32.3$ mm s^{-1}, and the Marangoni number is $Ma \sim 1700$. The dimensionless wavenumber and wave speed of SWI have values $k \sim O(0.3)$ and $c \sim O(0.6)$, while those of CI have values $k \sim O(1)$ and $c \sim O(0.15)$.

In table 7, we list the critical wavenumbers and wave speeds in the droplet migration when SWI and CI have the same Ma_c. For $Pr = 19.1$, the k and c values of SWI are of the same order as those in the experiment. The wave speed of CI is much smaller than that in the experiment. However, it has the same order as that in the theoretical analysis for the return flow (Smith & Davis 1983*a*). Both the experiment and our analysis suggest that the wavenumbers (wave speeds) of SWI are considerably smaller (larger) than those of CI.

5. Conclusion

In this paper, we examine the surface wave instability (SWI) in a droplet migration driven by the thermocapillary force. Both a Newtonian fluid and an Oldroyd-B fluid are considered. The results show that both convective instability (CI) and SWI can be found when the droplet has a deformable surface.

For the Newtonian fluid, when the Galileo number G or the surface-tension number S is large enough, CI is preferred, whose critical parameters are almost independent of G and S. For small Pr, the preferred modes of SWI include the streamwise and oblique waves, while for moderate and large Pr, only the streamwise wave of SWI is detected. The long-wave mode of SWI is preferred in some cases, whose properties are independent

Case	Type	k	c
1: $Ma_c = 198$, $Pr = 19.1$, $S = 1.04 \times 10^4$	SWI	0.116	1.87
	CI	2.51	0.03
2: $Ma_c = 14.5$, $Pr = 0.01$, $S = 1.65 \times 10^7$	SWI	0.224	0.845
	CI	1.41	0.018
3: $Ma_c = 72.1$, $Pr = 1$, $S = 3.16 \times 10^5$	SWI	0.102	1.539
	CI	2.12	0.086

Table 7. The critical wavenumbers and wave speeds when SWI and CI have the same Ma_c. Other parameters are $\zeta = 0.49$ and $Bo = 0$.

of Pr. The wavenumber of SWI is much smaller than that of CI, while the reverse is true for the wave speed.

Two kinds of perturbation flow fields are found. For the first one, there is no roll in the flow, and the hot spot is on the free surface. For the second one, there can be interior hot spots and rolls. The latter almost coincide with the isothermals. Energy analysis suggests that the energy of the long-wave mode comes from the shear stress induced by the surface deformation, the energy source for the mode with finite wavelength is the work done by Marangoni forces, while the energy from the basic flow becomes important in some cases at small Pr. The pressure on the surface and the buoyancy always lead to energy dissipation.

For the Oldroyd-B fluid, a small elasticity slightly changes the critical Marangoni number of SWI. When the elasticity number is large enough, the preferred mode changes from SWI to CI.

Funding. This work has been supported by the National Natural Science Foundation of China (Nos. 11872032, 11832013 and 11772344), Zhejiang Provincial Natural Science Foundation (No. LY21A020006), Key Research and Development Plan of Ningbo (2022Z213) and K.C. Wong Magna Fund in Ningbo University.

Declaration of interests. The authors report no conflict of interest.

Author ORCIDs.
Kai-Xin Hu https://orcid.org/0000-0001-7877-3386.

Author contributions. K.-X.H. made substantial contributions to the conception of the work, wrote the paper for important intellectual content and approved the final version to be published. He is accountable for all aspects of the work in ensuring that questions related to the accuracy or integrity of any part of the work are appropriately investigated and resolved. S.-N.Z. made contributions to the numerical computation and validation. Q.-S.C. provided editing and writing assistance.

Appendix A. The boundary conditions

The boundary conditions on the plane are:

$$\widehat{u} = \widehat{v} = \widehat{w} = \widehat{T} = 0, \quad z = 0. \tag{A1}$$

The boundary conditions at the deformed surface $z = 1 + \xi$ are projected onto $z = 1$ (Patne *et al.* 2021*a*),

$$\widehat{w} = \sigma\widehat{\xi} + \mathrm{i}\alpha U_0\widehat{\xi}, \tag{A2a}$$

$$\widehat{\tau}_{13} = -\mathrm{i}\alpha(\widehat{T} + \partial_z T_0\widehat{\xi}) + \mathrm{i}\alpha\bar{\tau}_{11}\widehat{\xi} - \frac{\partial\bar{\tau}_{13}}{\partial z}\widehat{\xi}, \tag{A2b}$$

$$\widehat{\tau}_{23} = -\mathrm{i}\beta(\widehat{T} + \partial_z T_0\,\widehat{\xi}), \tag{A2c}$$

$$-\widehat{p} + \widehat{\tau}_{33} = -\frac{(G\,Ca + \alpha^2 + \beta^2)}{Ca}\widehat{\xi} + 2\mathrm{i}\alpha\bar{\tau}_{13}\,\widehat{\xi}, \tag{A2d}$$

$$\mathrm{D}\widehat{T} + (-\mathrm{i}\alpha\partial_x T_0 + \partial_z^2 T_0)\widehat{\xi} = 0. \tag{A2e}$$

For the Newtonian fluid, $\bar{\tau}_{11} = 0$ and $\bar{\tau}_{13} = \mathrm{D}U_0$, (A2*a*)–(A2*e*) agree with (2.11*b*)–(2.11*f*) in Patne *et al.* (2020). In the derivation of the boundary condition for the normal stress, we neglect the effect caused by the variable surface tension. This requires

$$Ca \times 2\pi/k \ll 1, \tag{A3}$$

which means that the surface tension does not change much over the characteristic wavelength of a disturbance (Smith & Davis 1983*b*).

References

Bach, C. & Schwabe, D. 2015 Surface waves in thermocapillary flow-revisited. *Eur. Phys. J.: Spec. Top.* **224** (2), 319–340.

Bird, R.B., Armstrong, R.C. & Hassager, O. 1987 *Dynamics of Polymeric Liquids, Volume 1: Fluid Mechanics*. John Wiley & Sons, Inc.

Brochard, F. 1989 Motions of droplets on solid surfaces induced by chemical or thermal gradients. *Langmuir* **5**, 432–438.

Brzoska, J.B., Brochard-Wyart, F. & Rondelez, F. 1993 Motions of droplets on hydrophobic model surfaces induced by thermal gradients. *Langmuir* **9** (8), 2220–2224.

Chan, C.L. & Chen, C.F. 2010 Effect of gravity on the stability of thermocapillary convection in a horizontal fluid layer. *J. Fluid Mech.* **647**, 91–103.

Chen, J.Z., Darhuber, A.A., Troian, S.M. & Wagner, S. 2004 Capacitive sensing of droplets for microfluidic devices based on thermocapillary actuation. *Lab on a Chip* **4** (5), 473–480.

Chen, J.Z., Troian, S.M., Darhuber, A.A. & Wagner, S. 2005 Effect of contact angle hysteresis on thermocapillary droplet actuation. *J. Appl. Phys.* **97** (1), 014906.

Dai, Q.W., Huang, W., Wang, X.L. & Khonsari, M.M. 2018 Ringlike migration of a droplet propelled by an omnidirectional thermal gradient. *Langmuir* **34** (13), 3806–3812.

Dai, Q.W., Huang, W., Wang, X.L. & Khonsari, M.M. 2021 Directional interfacial motion of liquids: fundamentals, evaluations, and manipulation strategies. *Tribol. Intl* **154**, 106749.

Dai, Q.W., Ji, Y.J., Huang, W. & Wang, X.L. 2019 On the thermocapillary migration on radially micro-grooved surfaces. *Langmuir* **35** (28), 9169–9176.

Dai, Q.W., Khonsari, M.M., Shen, C., Huang, W. & Wang, X. 2016 Thermocapillary migration of liquid droplets Induced by a unidirectional thermal gradient. *Langmuir* **32** (30), 7485–7492.

Darhuber, A.A., Davis, J.M., Troian, S.M. & Reisner, W.W. 2003 Thermocapillary actuation of liquid flow on chemically patterned surfaces. *Phys. Fluids* **15** (5), 1295–1304.

Darhuber, A.A., Valentino, J.P. & Troian, S.M. 2010 Planar digital nanoliter dispensing system based on thermocapillary actuation. *Lab on a Chip* **10** (8), 1061–1071.

Davis, S.H. 1987 Thermocapillary instabilities. *Annu. Rev. Fluid Mech.* **19** (1), 403–435.

Duan, L., Kang, Q. & Hu, W.R. 2006 Characters of surface deformation and surface wave in thermal capillary convection. *Sci. China Ser.* E **49** (5), 601–610.

Duffar, T. 2010 *Crystal Growth Processes Based on Capillarity*. John Wiley & Sons, Ltd.

Ford, M.L. & Nadim, A. 1994 Thermocapillary migration of an attached drop on a solid surface. *Phys. Fluids* **6** (9), 3183–3185.

Hu, K.X., He, M. & Chen, Q.S. 2016 Instability of thermocapillary liquid layers for Oldroyd-B fluid. *Phys. Fluids* **28** (3), 033105.

Hu, K.X., He, M., Chen, Q.S. & Liu, R. 2018 Effect of gravity on the stability of viscoelastic thermocapillary liquid layers. *Intl J. Heat Mass Transfer* **123**, 776–786.

Hu, K.X., Peng, J. & Zhu, K.Q. 2012 The linear stability of plane Poiseuille flow of Burgers fluid at very low Reynolds numbers. *J. Non-Newtonian Fluid Mech.* **167**, 87–94.

Hu, K.X., Yan, C.Y. & Chen, Q.S. 2019 Instability of thermocapillary–buoyancy convection in droplet migration. *Phys. Fluids* **31** (12), 122101.

KARBALAEI, A., KUMAR, R. & CHO, H.J. 2016 Thermocapillarity in microfluidics – a review. *Micromachines* **7** (1), 13.

LAPPA, M. 2009 *Thermal Convection: Pattern, Evolution and Stability*. John Wiley and Sons.

LI, Y.R., IMAISHI, N., AZAMI, T. & HIBIYA, T. 2004 Three-dimensional oscillatory flow in a thin annular pool of silicon melt. *J. Cryst. Growth* **260** (1-2), 28–42.

LIU, H.H. & ZHANG, Y.H. 2015 Modelling thermocapillary migration of a microfluidic droplet on a solid surface. *J. Comput. Phys.* **280**, 37–53.

PATNE, R., AGNON, Y. & ORON, A. 2020 Thermocapillary instabilities in a liquid layer subjected to an oblique temperature gradient: effect of a prescribed normal temperature gradient at the substrate. *Phys. Fluids* **32** (11), 112109.

PATNE, R., AGNON, Y. & ORON, A. 2021*a* Thermocapillary instabilities in a liquid layer subjected to an oblique temperature gradient. *J. Fluid Mech.* **906**, A12.

PATNE, R., AGNON, Y. & ORON, A. 2021*b* Thermocapillary instability in a viscoelastic liquid layer under an imposed oblique temperature gradient. *Phys. Fluids* **33** (1), 012107.

PÉREZ-GARCÍA, C. & CARNEIRO, G. 1991 Linear stability analysis of Bénard–Marangoni convection in fluids with a deformable free surface. *Phys. Fluids* A*: Fluid Dyn.* **3** (2), 292–298.

PRATAP, V., MOUMEN, N. & SUBRAMANIAN, R.S. 2008 Thermocapillary motion of a liquid drop on a horizontal solid surface. *Langmuir* **24** (9), 5185–5193.

RILEY, R.J. & NEITZEL, G.P. 1998 Instability of thermocapillary–buoyancy convection in shallow layers. Part 1. Characterization of steady and oscillatory instabilities. *J. Fluid Mech.* **359**, 143–164.

SCHATZ, M.F. & NEITZEL, G.P. 2001 Experiments on thermocapillary instabilities. *Annu. Rev. Fluid Mech.* **33** (1), 93–127.

SCHMID, P.J. & HENNINGSON, D.S. 2001 *Stability and Transition in Shear Flows*. Springer.

SELVA, B., MIRALLES, V., CANTAT, I. & JULLIEN, M.C. 2010 Thermocapillary actuation by optimized resistor pattern: bubbles and droplets displacing, switching and trapping. *Lab on a Chip* **10** (14), 1835–1840.

SHANKAR SUBRAMANIAN, R. AND BALASUBRAMANIAM, R. 2005 *The Motion of Bubbles and Drops in Reduced Gravity*. Cambridge University Press.

SMITH, M.K. 1995 Thermocapillary migration of a two-dimensional liquid droplet on a solid-surface. *J. Fluid Mech.* **294**, 209–230.

SMITH, M.K. & DAVIS, S.H. 1983*a* Instabilities of dynamic thermocapillary liquid layers. Part 1. Convective instabilities. *J. Fluid Mech.* **132**, 119–144.

SMITH, M.K. & DAVIS, S.H. 1983*b* Instabilities of dynamic thermocapillary liquid layers. Part 2. Surface-wave instabilities. *J. Fluid Mech.* **132**, 145–162.

SURESHKUMAR, R. & BERIS, A.N. 1995 Linear stability analysis of viscoelastic Poiseuille flow using an Arnoldi-based orthogonalization algorithm. *J. Non-Newtonian Fluid Mech.* **56** (2), 151–182.

VALENTINO, J.P., TROIAN, S.M. & WAGNER, S. 2005 Microfluidic detection and analysis by integration of thermocapillary actuation with a thin-film optical waveguide. *Appl. Phys. Lett.* **86** (18), 184101.

WANSCHURA, M., SHEVTSOVA, V.M., KUHLMANN, H.C. & RATH, H.J. 1995 Convective instability mechanisms in thermocapillary liquid bridges. *Phys. Fluids* **7** (5), 912–925.

WU, Z.B. 2018 Steady thermocapillary migration of a droplet in a uniform temperature gradient combined with a radiation energy source at large Marangoni numbers. *Phys. Rev.* E **98** (1), 013110.

YAN, C.Y., HU, K.X. & CHEN, Q.S. 2018 Thermocapillary instabilities of liquid layers on an inclined plane. *Phys. Fluids* **30** (8), 082101.

ZHU, P., ZHOU, B., DUAN, L. & KANG, Q. 2011 Characteristics of surface oscillation in thermocapillary convection. *Exp. Therm. Fluid Sci.* **35** (7), 1444–1450.